A High-Order Finite-Volume Scheme for Large-Eddy Simulation of Turbulent Premixed Flames

L. Tobaldini Neto [*] and C. P. T. Groth [†]

University of Toronto Institute for Aerospace Studies

4925 Dufferin Street, Toronto, ON, M3H 5T6, Canada

A novel, parallel, high-order, central essentially non-oscillatory (CENO), cell-centered, finite-volume scheme is developed and applied to large-eddy simulation (LES) of turbulent premixed flames. The high-order CENO finite-volume scheme is applied to the solution of the Favre-filtered Navier-Stokes equations governing turbulent flows of a fully-compressible reactive mixture on three-dimensional, multi-block, body-fitted, computational mesh consisting of hexahedral volume elements. Unlike standard ENO schemes, which require solution reconstruction on multiple stencils, the CENO method uses a hybrid reconstruction approach based on a fixed central stencil, thereby avoiding the complexities of other ENO schemes while providing high-order accuracy at relatively lower computational cost. The CENO discretization of the inviscid fluxes combines an unlimited high-order k-exact least-squares reconstruction technique based on the optimal central stencil with a monotonicity-preserving, limited, linear, reconstruction algorithm. Switching in the hybrid procedure is determined by a smoothness indicator such that the unlimited high-order reconstruction is retained for smooth solution content that is fully resolved and reverts to the limited lower-order scheme, enforcing solution monotonicity, for regions with abrupt variations (i.e., discontinuities and under-resolved regions). The high-order viscous fluxes are computed to the same order of accuracy as the hyperbolic fluxes based on a k-order accurate cell interface gradient derived from the unlimited, cell-centered, reconstruction. The proposed cell-centered finite-volume scheme is formulated for three-dimensional multi-block mesh consisting of generic hexahedral cells and applied to LES of premixed flames.For the reactive cases flows of interest, a flamelet-based subfilter-scale (SFS) model is used to describe the unresolved influences of interaction between the turbulence and combustion. This SFS combustion model is based on a presumed conditional moment (PCM) approach in conjunction with flame prolongation of intrinsic low-dimensional manifold (FPI) tabulated chemistry. Numerical results are discussed for a freely propagating flame in an isotropic turbulence field and for a laboratory-scale lean premixed methane-air Bunsen-type flame. The performance of the proposed high-order scheme for turbulent reactive flows is discussed.

I.   Introduction and Motivation

As indicated by Bilger,[1] numerical combustion modeling of practical combustion systems with fully turbulent flows and complex geometries is still at an initial stage and is really only used peripherally in the industrial development of new and/or advanced combustor technology. The simulation of practical, real-geometry combustors, with complete or multiple-step treatment of chemical reaction mechanisms, is still a very computationally demanding task. High-order spatial and temporal discretization methods offer the potential to reduce the computational costs required to obtain accurate predictions of such simulations as compared to standard lower-order (second-order) methods. Nevertheless, efficient, universally-applicable, high-order discretizations remain somewhat illusive, especially for more arbitrary three-dimensional and/or unstructured computational meshes and for the prediction of physically complex flows as encountered in many turbulent combustion flows.

---

[*]Ph.D. Candidate, Product Development Engineer at Embraer S.A. (Brazil), tobaldini@utias.utoronto.ca
[†]Professor, Senior Member AIAA, groth@utias.utoronto.ca

American Institute of Aeronautics and Astronautics

In terms of spatial discretization methods for reactive flows, recent efforts have concentrated on high-order finite-difference approaches and on intermediate third-order finite-volume approaches with simplified (one- or two-step) chemistry. For example, high-order methods are conventionally reserved for Direct Numerical Simulation (DNS) on simpler structured grids and practical Large Eddy Simulation (LES) applied to combustion is generally second-order accurate.[2,3,4] Another example of high-order LES using finite-difference methods to simulate methane combustion is the work of Yaldizli *et al*,[5] where the filtered mass density function methodology is employed as a Subgrid Scale (SGS) closure for the LES model. Franzelli *et al*[6] uses a third-order finite-element solver to study combustion instabilities on a swirled combustor at different equivalence ratios. In another effort, Wang *et al*[7] developed a three-dimensional (3D) parallel solver using fifth-order weighted essentially non-oscillatory (WENO) finite-difference scheme to perform simulation of gaseous detonations. One example of second-order LES using a finite-volume scheme applied to combustion is given in Fureby.[8] Despite these efforts, certainly further research is required if the potential of high-order methods for reactive flow simulations is to be fully realized.

II.   Scope of the Present Study

In the present study, a novel, parallel, high-order, central essentially non-oscillatory (CENO), cell-centered, finite-volume scheme is developed and applied to LES of turbulent premixed flames. The high-order CENO finite-volume scheme of Ivan and Groth[9,10] is applied to the solution of the Favre-filtered Navier-Stokes equations governing turbulent flows of a fully-compressible reactive mixture on three-dimensional, multi-block, body-fitted, computational mesh consisting of hexahedral volume elements. Unlike standard ENO schemes, which require solution reconstruction on multiple stencils, the CENO method uses a hybrid reconstruction approach based on a fixed central stencil, thereby avoiding the complexities of other ENO schemes while providing high-order accuracy at relatively lower computational cost. The CENO discretization of the inviscid fluxes combines an unlimited high-order k-exact least-squares reconstruction technique based on the optimal central stencil with a monotonicity-preserving, limited, linear, reconstruction algorithm. Switching in the hybrid procedure is determined by a smoothness indicator such that the unlimited high-order reconstruction is retained for smooth solution content that is fully resolved and reverts to the limited lower-order scheme, enforcing solution monotonicity, for regions with abrupt variations (i.e., discontinuities and under-resolved regions). The high-order viscous fluxes are computed to the same order of accuracy as the hyperbolic fluxes based on a k-order accurate cell interface gradient derived from the unlimited, cell-centered, reconstruction. One major advantage of the proposed finite-volume based approach is that its extension to unstructured mesh is very straightforward and preserves most of the implementation used for hexahedral cells. The application of the CENO scheme to three-dimensional unstructured mesh was previously considered by Charest *et al.*[11] The high-order scheme is formulated here for three-dimensional multi-block mesh consisting of generic hexahedral cells (faces not necessarily planar) and, in order to demonstrate the capabilities of the high-order method, LES of freely propagating premixed flames in an isotropic turbulent field and a laboratory-scale lean premixed Bunsen-type flame will be considered. For the latter, a gaseous fuel, methane, is considered and a flamelet-based subfilter-scale (SFS) LES model is used to describe the unresolved influences of interaction between the turbulence and combustion. The SFS combustion model is based on a presumed conditional moment (PCM) approach in conjunction with flame prolongation of intrinsic low-dimensional manifold (FPI) tabulated chemistry.

In what follows, details of the proposed high-order CENO scheme are discussed and described, including a description the PCM-FPI turbulence-chemistry interaction combustion model for premixed flames. Numerical results are presented and discussed for several non-reactive flow problems as well as the freely-propagating and Bunsen-type premixed flames.

III.   Filtered Navier-Stokes Equations for Compressible Reactive Mixtures

The Navier-Stokes conservation equations for a compressible reactive mixture of thermally perfect gases can be Favre-filtered, providing the equations for variables, $\bar{\varphi}$ or $\tilde{\varphi}$. The resulting Favre-filtered form of the conservation equations for mass, momentum, total energy, and species mass fractions, along with the

equation of state used here in the LES of turbulent reactive flows are given by

$$\frac{\partial \bar{\rho}}{\partial t} + \frac{\partial (\bar{\rho} \tilde{u}_j)}{\partial x_j} = 0 \,, \tag{1}$$

$$\frac{\partial (\bar{\rho} \tilde{u}_i)}{\partial t} + \frac{\partial (\bar{\rho} \tilde{u}_i \tilde{u}_j + \delta_{ij} \bar{p})}{\partial x_j} - \frac{\partial \check{\tau}_{ij}}{\partial x_j} = \bar{\rho} g_i + \underbrace{\frac{\partial \sigma_{ij}}{\partial x_j}}_{\mathbf{I}} + \underbrace{\frac{\partial (\bar{\tau}_{ij} - \check{\tau}_{ij})}{\partial x_j}}_{\mathbf{II}} \,, \tag{2}$$

$$
\begin{aligned}
\frac{\partial (\bar{\rho} \tilde{E})}{\partial t} + \frac{\partial [(\bar{\rho} \tilde{E} + \bar{p}) \tilde{u}_j]}{\partial x_j} - \frac{\partial (\check{\tau}_{ij} \tilde{u}_i)}{\partial x_j} + \frac{\partial \check{q}_j}{\partial x_j} \; = \; & \bar{\rho} \tilde{u}_i g_i - \underbrace{\frac{\partial [\bar{\rho} (\widetilde{h_s u_j} - \check{h}_s \tilde{u}_j)]}{\partial x_j}}_{\mathbf{III}} \\
& + \underbrace{\frac{\partial (\overline{\tau_{ij} u_i} - \check{\tau}_{ij} \tilde{u}_i)}{\partial x_j}}_{\mathbf{IV}} - \underbrace{\frac{\partial (\bar{q}_j - \check{q}_j)}{\partial x_j}}_{\mathbf{V}} \\
& - \frac{1}{2} \underbrace{\frac{\partial [\bar{\rho} (\widetilde{u_j u_i u_i} - \tilde{u}_j \widetilde{u_i u_i})]}{\partial x_j}}_{\mathbf{VI}} \\
& - \underbrace{\frac{\partial [\sum_{\alpha=1}^{N} \Delta h_{f_\alpha}^0 \bar{\rho} (\widetilde{Y_\alpha u_j} - \tilde{Y}_\alpha \tilde{u}_j)]}{\partial x_j}}_{\mathbf{VII}} \,,
\end{aligned}
\tag{3}
$$

$$\frac{\partial (\bar{\rho} \tilde{Y}_\alpha)}{\partial t} + \frac{\partial (\bar{\rho} \tilde{Y}_\alpha \tilde{u}_j)}{\partial x_j} + \frac{\partial \check{\mathcal{J}}_{j,\alpha}}{\partial x_j} = - \underbrace{\frac{\partial [\bar{\rho} (\widetilde{Y_\alpha u_j} - \tilde{Y}_\alpha \tilde{u}_j)]}{\partial x_j}}_{\mathbf{VIII}} - \underbrace{\frac{\partial (\bar{\mathcal{J}}_{j,\alpha} - \check{\mathcal{J}}_{j,\alpha})}{\partial x_j}}_{\mathbf{IX}} + \underbrace{\bar{\dot{\omega}}_\alpha}_{\mathbf{X}} \,, \tag{4}$$

$$\bar{p} = \bar{\rho} \check{R} \tilde{T} + \underbrace{\sum_{\alpha=1}^{N} R_\alpha \bar{\rho} (\widetilde{Y_\alpha T} - \tilde{Y}_\alpha \tilde{T})}_{\mathbf{XI}} \,, \tag{5}$$

where

$$\sigma_{ij} = -\bar{\rho} \left(\widetilde{u_i u_j} - \tilde{u}_i \tilde{u}_j \right) \,, \tag{6}$$

is the SFS stress tensor. The Favre-filtered total energy takes the form

$$\tilde{E} = \check{h}_s - \frac{\bar{p}}{\bar{\rho}} + \sum_{\alpha=1}^{N} \Delta h_{f_\alpha}^0 \tilde{Y}_\alpha + \frac{1}{2} \tilde{u}_i \tilde{u}_i + k_\Delta \,, \tag{7}$$

where

$$k_\Delta = \frac{1}{2} \left(\widetilde{u_i u_i} - \tilde{u}_i \tilde{u}_i \right) \,, \tag{8}$$

is the SFS turbulent kinetic energy.

The effects of the subfilter scales appear in the filtered total energy, $\tilde{E}$, the filtered equation of state and the right-hand-sides of the governing continuity, momentum, energy and species mass fraction equations (i.e., terms $\mathbf{I}, \ldots, \mathbf{XI}$). The symbol (̌) is used to indicate the evaluation of expressions in terms of filtered variables, i.e., $\check{R} = R(\tilde{Y}_\alpha)$, $\check{h}_s = h_s(\tilde{Y}_\alpha, \tilde{T})$, and so on. The fluxes $\check{\tau}_{ij}$, $\check{q}_j$, and $\check{\mathcal{J}}_{j,\alpha}$ are expressed as

$$\check{\tau}_{ij} = 2 \check{\mu} \left(\check{S}_{ij} - \frac{1}{3} \delta_{ij} \check{S}_{ll} \right) \,, \tag{9}$$

$$\check{q}_j = -\check{\lambda} \frac{\partial \tilde{T}}{\partial x_j} - \bar{\rho} \sum_{\alpha=1}^{N} \check{h}_\alpha \check{D}_\alpha \frac{\partial \tilde{Y}_\alpha}{\partial x_j} \,, \tag{10}$$

$$\check{\mathcal{J}}_{j,\alpha} = -\bar{\rho} \check{D}_\alpha \frac{\partial \tilde{Y}_\alpha}{\partial x_j} \,, \tag{11}$$

American Institute of Aeronautics and Astronautics

where $\check{S}_{ij} = \frac{1}{2}\left(\partial \tilde{u}_i/\partial x_j + \partial \tilde{u}_j/\partial x_i\right)$, is the strain rate tensor calculated with the Favre-filtered velocity. The temperature used for the molecular transport coefficients $\check{\mu}$, $\check{\lambda}$, and $\check{D}_\alpha$ calculations is $\tilde{T}$.

For the non-reactive flows considered, the standard Smagorinsky SFS model[12] is used to represent the unresolved turbulence. For the reactive flow simulations a one-equation eddy-viscosity model based on a transport equation for the SFS turbulent kinetic energy, k_Δ [13,14] is used. The SFS stresses are modelled as:

$$\sigma_{ij} = 2\bar{\rho}\nu_{\mathrm{t}}\left(\check{S}_{ij} - \frac{1}{3}\delta_{ij}\check{S}_{ll}\right) - \bar{\rho}\frac{2}{3}\delta_{ij}k_\Delta\,, \tag{12}$$

where

$$\nu_{\mathrm{t}} = C_\nu k_\Delta^{1/2}\Delta\,, \tag{13}$$

and the value of k_Δ is obtained from the modelled transport equation

$$\frac{\partial(\bar{\rho}k_\Delta)}{\partial t} + \frac{\partial(\bar{\rho}k_\Delta\tilde{u}_i)}{\partial x_i} = \sigma_{ij}\check{S}_{ij} - \frac{C_\epsilon\bar{\rho}k_\Delta^{3/2}}{\Delta} + \frac{\partial}{\partial x_i}\left[\bar{\rho}\left(\check{\nu} + \frac{\nu_{\mathrm{t}}}{\zeta^*}\right)\frac{\partial k_\Delta}{\partial x_i}\right]\,, \tag{14}$$

where $\check{\nu}$ is the mixture kinematic viscosity evaluated in terms of filtered variables $(\check{\nu} = \check{\mu}/\bar{\rho})$.

IV. PCM-FPI Model

The PCM-FPI combustion model is used here to describe the interaction of the unresolved turbulence and chemistry when performing LES of turbulent reactive flows and provide predictions of the chemical reaction rates. The LES implementation of the PCM-FPI model used in the present work was developed and successfully demonstrated by Hernàndez-Pérez et al[15] and by Shahbazian et al[16] for freely propagating turbulent premixed flames as well as Bunsen-type turbulent premixed flames. This SFS model is selected because it represents a reasonable trade-off between accuracy and cost in the representation of complex chemistry.

A. Tabulated Chemistry - FPI

Since the cost of performing full chemistry simulation, including detailed kinetics, in realistic computations is very high, reduction techniques have been an important field of research in combustion simulation. The Flame Prolongation of ILDM (FPI) tabulation method was proposed by Gicquel et al[17] as an extension to the Intrinsic Low Dimensional Manifold (ILDM) approach.[18] The goal is to retain the benefits of using complex chemistry results, by building databases based on detailed simulations of simple flames. Premixed steady-state one-dimensional laminar flames provide the basis for the FPI tabulations.[15] In the present work, premixed steady-state one-dimensional laminar flames are solved by the software Cantera[19] using the GRI-3.0 mechanism.[20]

For problems having a low Mach number, with Lewis number around unity and adiabatic boundaries, a single progress variable suffices to describe the complete thermochemical state of the system.[21] Premixed flame solution quantities are then related to this single progress variable, Y_{c}. The choice of this variable should be carefully done so that a one-to-one correspondence between Y_{c} and every flame property exists.[22] For example, Fiorina et al[23] indicate that for methane-air combustion (our particular case of study here), $Y_{\mathrm{c}} = Y_{\mathrm{CO}} + Y_{\mathrm{CO}_2}$ is an appropriate choice and is used here. These findings have also been confirmed in other previous studies.[15,24,16]

In the FPI approach applied to premixed flames, numerical solutions for a set of one-dimensional freely propagating laminar premixed flames are computed and the flame quantities are stored on a look-up table in terms of the reaction progress variable Y_{c}, and a mixture fraction characterizing the equivalence ratio Y_{z}. A property φ^{P} (species mass fractions, reaction rates, etc.) of unstrained premixed flames at a given equivalence ratio may be tabulated either in (x, Y_{z}) or in $(Y_{\mathrm{c}}, Y_{\mathrm{z}})$. The FPI table can then be expressed as[25]

$$\varphi_j^{\mathrm{FPI}}(Y_{\mathrm{z}}, Y_{\mathrm{c}}) = \varphi_j^{\mathrm{P}}(Y_{\mathrm{z}}, x)\,. \tag{15}$$

Another important characteristic of the FPI approach is that the number of species retained in the tabulations may be reduced when building the tables so as to optimize the table size. In the present study, 10 species were selected for tabulation which were deemed more relevant to the combustion process based on their individual contributions to the total mass, energy and heat release for the complete mixture representation.

American Institute of Aeronautics and Astronautics

B.   Presumed Conditional Moment

Probability density functions (PDF) methods have shown to be successful even in some very complex applications. Examples include their ability to capture strong turbulence-chemistry interactions even in flames with strong local extinction/reignition, and their ability to capture strong turbulence-radiation interactions in luminous flames.[26]

The presumed conditional moment (PCM)[27,28] combined with the flame prolongation of intrinsic low-dimensional manifold (FPI)[17] chemistry tabulation technique, is a closure approach that uses a presumed PDF for fluctuating subfilter-scale quantities and incorporates tabulated complex chemistry from simple prototype combustion problems. When turbulent premixed combustion is considered, look-up tables of filtered terms associated with chemistry are built from laminar premixed flamelets. Also, the PCM-FPI model is rather general and can be applied to all three combustion regimes: premixed, non-premixed, and partially premixed flames.

Employing a statistical approach, the Favre-filtered reaction rate for a species α can be calculated by integrating the laminar reaction rate, $\dot{\omega}_\alpha$, with a joint subfilter PDF, $\tilde{P}$, as follows:

$$\tilde{\dot{\omega}}_\alpha = \int_{T^*}\int_{Y_1^*}\dots\int_{Y_N^*}\dot{\omega}_\alpha(T^*, Y_1^*, \dots, Y_N^*)\tilde{P}(T^*, Y_1^*, \dots, Y_N^*)\,\mathrm{d}Y_N^*\dots\mathrm{d}Y_1^*\mathrm{d}T^* . \tag{16}$$

The above description can be simplified if the laminar reaction rate is assumed to be characterized by two parameters: the mixture fraction, Z, and the progress variable, c, as provided by the FPI tabulated chemistry. The mixture fraction characterizes mixing between fuel and oxidizer (Z is related to the equivalence ratio, ϕ), whereas the progress variable tracks the evolution of the reactions. Both variables take on values between zero and unity. The filtered reaction rate can then be re-expressed as

$$\tilde{\dot{\omega}}_\alpha = \int_0^1\int_0^1\dot{\omega}_\alpha(c^*, Z^*)\tilde{P}(c^*, Z^*)\,\mathrm{d}c^*\mathrm{d}Z^* . \tag{17}$$

On the other hand, the joint subfilter PDF can be also written as $\tilde{P}(c^*, Z^*) = \tilde{P}(c^*|Z^*)\tilde{P}(Z^*)$. By analyzing DNS data, Vervisch[29] have shown that the conditional PDF does not hage a strong dependence on the mixture fraction, suggesting that $\tilde{P}(c^*|Z^*) \approx \tilde{P}(c^*)$. Assuming, $\tilde{P}(c^*|Z^*) = \tilde{P}(c^*)$, the filtered reaction rate can then be evaluated using

$$\tilde{\dot{\omega}}_\alpha = \int_0^1\int_0^1\dot{\omega}_\alpha(c^*, Z^*)\tilde{P}(c^*)\tilde{P}(Z^*)\,\mathrm{d}c^*\mathrm{d}Z^* . \tag{18}$$

It follows that the filtered conditional moment $\overline{(\dot{\omega}|Z^*)}$ is given by

$$\overline{(\dot{\omega}|Z^*)} = \int_0^1\dot{\omega}_\alpha(c^*, Z^*)\tilde{P}(c^*)\mathrm{d}c^* . \tag{19}$$

In this sense, the PCM approach can be viewed as a simplified version of the Conditional Moments Closure (CMC) method, in that conditional moments are also employed, but instead of solving transport equations for the moments, they are presumed. The coupling of the laminar flamelet modeled reactions (tabulated) and the filtered equations is made by solving two additional transport equations to characterize the shape of the PDF: one equation for the progress of reaction variable Y_c and another for the variance of the progress variable Y_{c_v}.[28,30,22]

A β-PDF is generally used as the presumed probability density function for the progress variable in both premixed and non-premixed flames.[31,22,30,32] This was the choice for the present work mainly due to the comparative nature of the results presented and to be consistent with some legacy results. Besides the β-PDF, the Bray et al[33]'s laminar flame-based PDF and the modified laminar flame-based PDF of Jin et al[34] are available in the present computational framework. Particularly the latter has been considered to be a more appropriate choice for turbulent flames lying within the thin reaction zone regime and will be the choice for future studies.

In this work, the integration of the PDF's with the laminar solution is pre-computed and stored. So, given the local values of the progress of reaction variable Y_c scalar and the variance of the progress variable Y_{c_v} scalar, the pre-computed tables are accessed and the corresponding mass-fractions of each species is then retrieved. Alternatively one could also use the tables to retrieve the reaction rates and solve extra conservation equations for each species.

V.   High-Order Finite-Volume Spatial Discretization Scheme

A.   Weak Conservation Form of Governing Equations

The Favre-filtered form of the conservation equations for mass, momentum, total energy, and species mass fractions, along with the equation of state are used here in the LES of turbulent reactive flows given by Eqs. (1)–(4) above can be re-expressed in the following general weak conservation form using matrix-vector notation:

$$\frac{\partial \overline{\mathbf{U}}}{\partial t} + \vec{\nabla} \cdot \vec{\mathcal{F}} = \frac{\partial \overline{\mathbf{U}}}{\partial t} + \vec{\nabla} \cdot \vec{\mathcal{F}}^{\mathrm{I}}\left(\overline{\mathbf{U}}\right) - \vec{\nabla} \cdot \vec{\mathcal{F}}^{\mathrm{V}}\left(\overline{\mathbf{U}}, \vec{\nabla}\overline{\mathbf{U}}\right) = \overline{\mathbf{S}} \tag{20}$$

where $\overline{\mathbf{U}}$ is the vector of conserved solution variables and $\vec{\mathcal{F}}$ is the solution flux dyad. The flux dyad can be decomposed into two components and written as $\vec{\mathcal{F}} = \vec{\mathcal{F}}^{\mathrm{I}} - \vec{\mathcal{F}}^{\mathrm{V}}$ where $\vec{\mathcal{F}}^{\mathrm{I}} = \vec{\mathcal{F}}^{\mathrm{I}}(\overline{\mathbf{U}})$ contains the hyperbolic or inviscid components of the solution fluxes $\vec{\mathcal{F}}^{\mathrm{V}} = \vec{\mathcal{F}}^{\mathrm{V}}(\overline{\mathbf{U}}, \vec{\nabla}\overline{\mathbf{U}})$ contains the elliptic or viscous components of the fluxes. The latter depend on both the solution and its gradient.

B.   Semi-Discrete Form

Numerical solutions of Eq. (20) are sought here by applying a cell-centered, finite-volume, spatial discretization procedure. A semi-discrete form of the governing equations can be derived from the application of the finite-volume method to the integral form of Eq. (20) for cell (i, j, k) of a three-dimensional multi-block mesh composed of hexahedral volume elements. Using a N_G-point Gaussian quadrature numerical integration procedure to evaluate the solution flux along each of the N_f faces of the cell, the following semi-discrete form is obtained:

$$\frac{\mathrm{d}\overline{\mathbf{U}}_{ijk}}{\mathrm{d}t} = -\frac{1}{V_{ijk}} \sum_{l=1}^{N_f} \sum_{m=1}^{N_{GF}} \left(\omega_m \left(\vec{\mathcal{F}}^{\mathrm{I}} - \vec{\mathcal{F}}^{\mathrm{V}}\right) \cdot \hat{n}A\right)_{ijk,l,m} + \sum_{n=1}^{N_{GV}} (\omega_n \mathbf{S})_{i,j,k,n} = \overline{\mathbf{R}}_{ijk}\left(\overline{\mathbf{U}}\right), \tag{21}$$

where ω_m are the face quadrature weighting coefficients, ω_n are the volumetric quadrature weighting coefficients, A_l denotes the surface area of face l, and $\overline{\mathbf{R}}_{ijk}$ is the residual operator. After the evaluation of $\overline{\mathbf{R}}$, one can advance the solution in time, and therefore iteratively solve the time dependent problem that is described by the equations. It will be shown in section D that the same integration rule can be applied for a generic hexahedral element with a proper derivation of the quadrature points coordinates and weights. Referring to figure 1, the flux evaluation points on a given face in the hexahedral are illustrated for N_{GF}=4. Similar quadrature rules are used to determine the N_{GV} volumetric points.

The high-order finite-volume scheme implemented in this work employs four further steps based on the semi-discrete form presented above. They are:

1. **Solution Reconstruction**: Given the cell average values a functional is defined (Taylor series expansion polynomial) to represent the variation of the solution within one cell based on the cell itself and on its neighbours average solution;

2. **Flux Evaluation**: Fluxes are evaluated by reconstructing the cell solution at each quadrature point at the cell faces. Inviscid and Viscous Fluxes at one face are calculated by using the proper weights and coordinates given by the selected quadrature procedure (in this work Gauss-Legendre points and weights are used);

3. **Source Vector Evaluation**: The components of this vector are the terms that incorporate effects of turbulence and chemistry in the reacting flows. In the high-order spatial scheme the source terms integration is performed using a Gauss-Legendre quadrature approach, as defined in equation 26;

4. **Time marching**: Appropriate time marching scheme is used to update the cell-averaged values to the next time step, after the evaluation of $\overline{\mathbf{R}}$. A fourth-order Runge-Kutta (RK4) method is used for the high-order results presented here.

American Institute of Aeronautics and Astronautics

C. k-**Exact Least-Squares Reconstruction**

The high-order CENO reconstruction scheme of Ivan and Groth[9, 10] uses a k-exact least-squares reconstruction technique developed by Barth and Fredrickson[35] and Barth.[36] The reconstructed solution is thus given by the kth-order Taylor series expansion of the solution variable U, about the cell center. For the Favre-filtered Navier-Stokes equations used in this work, spatial accuracy of the scheme corresponds to the order of the reconstruction polynomial, k.

The kth-order Taylor series of the spatial distribution of a solution quantity, U_{ijk}, inside the cell with index ijk, about the cell-centroid $(x_{ijk}, y_{ijk}, z_{ijk})$ can be expressed as:

$$U_{ijk}^k(x,y,z) = \sum_{\substack{p_1=0 \\ (p_1+p_2+p_3 \leq k)}}^{k} \sum_{p_2=0}^{k} \sum_{p_3=0}^{k} (x - x_{ijk})^{p_1} (y - y_{ijk})^{p_2} (z - z_{ijk})^{p_3} D_{p_1 p_2 p_3}, \qquad (22)$$

The constant coefficients, $D_{p_1 p_2 p_3}$, are referred in this work as as the *unknown derivatives* and their number varies according to the order of the reconstruction. It can be easily shown that there are 10 unknown derivatives for a second-order (piecewise quadratic) reconstruction, 20 unknowns for a third-order (piecewise cubic) reconstruction and 35 for a fourth-order (piecewise quartic) reconstruction.

A least-squares problem is solved based on information of the neighbouring cells (stencil) in order to calculate the unknown derivatives. Barth and Fredrickson[35] impose the following constraints to this problem which are also used in this work: (i) the reconstruction should conserve the mean value in the cell to which its applied; (ii) the reconstruction should represent polynomials of degree $\delta \leq k$ exactly, and (iii) the reconstruction should have a compact support from the stencils.

In order to obtain a determined or overdetermined set of equations to solve for the unknown derivatives, the number of neighbours considered in the stencil must be at least equal to the number of unknown derivatives. The more information we take from the surrounding neighbours, the more robust the reconstruction, but at the same time it is not desirable to make the overdetermined system larger than necessary.[37] For most of the high-order (4th order) reconstruction results to be presented here a 56 neighbours stencil was used.

The smoothness indicator, S, used to determine whether a flow variable in cell (i, j, k) is deemed under-resolved or non-smooth, is computed as following:[37, 38]

$$\mathcal{S} = \frac{\alpha}{\max(1-\alpha, \epsilon)} \frac{\mathcal{N}_{\text{SOS}} - \mathcal{N}_D}{\mathcal{N}_D - 1}, \qquad \alpha = 1 - \frac{\sum_{\gamma}\sum_{\delta}\sum_{\zeta}(u_{\gamma\delta\zeta}^K(\vec{X}_{\gamma\delta\zeta}) - u_{ijk}^K(\vec{X}_{\gamma\delta\zeta}))^2}{\sum_{\gamma}\sum_{\delta}\sum_{\zeta}(u_{\gamma\delta\zeta}^K(\vec{X}_{\gamma\delta\zeta}) - \bar{u}_{ijk})^2}, \qquad (23)$$

where the ranges of the indices (γ, δ, ζ) are taken to include either the whole or a subset of the supporting reconstruction stencil for cell (i, j, k). The smoothness indicator can be interpreted as a comparison between 1) the reconstructed value in a neighbour cell given by this cell's own reconstruction and 2) the reconstructed value in a neighbour cell given by the central cell reconstruction.

D. **Hexahedral Elements and Trilinear Transformation**

In order to obtain high-order accuracy on generic hexahedral volumes the non-planar faces must be carefully treated with regard to all geometric operations affecting the numerical procedure such as flux integration and calculation of geometric properties (e.g., area, volume, centroid, moments etc.). The solution adopted in the present work is to define general hexahedral cells with a trilinear description of the faces, which allows us to perform all geometric computations with high-order accuracy by transforming the element to a reference cubic cell. According to Ivan *et al*,[38] the use of a standard trilinear face representation[39, 40] has significant advantages when the required number of flux integration points is taken into account, in comparison to a triangulation alternative.

1. *Trilinear Transformation*

In order to extend the CENO scheme for Cartesian structured meshes to hexahedral cells a trilinear transformation[40] is adopted to map a hexahedron from physical space into a reference unitary cube in the canonical
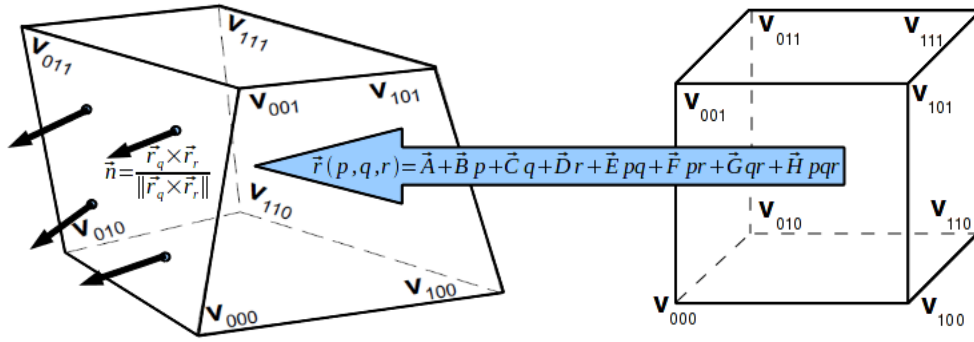
American Institute of Aeronautics and Astronautics

Figure 1. A general hexahedral cell in physical space mapped into a reference cube by applying a trilinear transformation $\vec{r}(p, q, r)$, as illustrated by Ivan *et al*[38]

space. Figure 1 illustrates a generic hexahedron (with non-planar faces) being mapped by a trilinear transformation applied to a cube.

$$\vec{r}(p, q, r) = \vec{A} + \vec{B}p + \vec{C}q + \vec{D}r + \vec{E}pq + \vec{F}pr + \vec{G}qr + \vec{H}pqr \,, \tag{24}$$

where p, q and r are Cartesian coordinates in the canonical space of the reference cube and $\vec{A}$, $\vec{B}$, $\vec{C}$, $\vec{D}$, $\vec{E}$, $\vec{F}$, $\vec{G}$ and $\vec{H}$ are the transformation vector coefficients that are computed by imposing the one-to-one correspondence between the vertices of the hexahedron and those of the reference cube. Once the transformation coefficients are determined, any local or integrated quantities involving the geometry of the hexahedron (e.g., centroid, volume, face normals, volumetric or face integrals of arbitrary functions, etc.) can be computed by carrying out the required evaluations within the reference cube.[39,41] For example, to evaluate a volumetric integral of a continuous smooth function, $g(\vec{X})$, over a control volume $\mathcal{V}_{ijk}$, $\mathcal{I} = \iiint_{\mathcal{V}_{ijk}} g(\vec{X}) \mathrm{d}v$, the variables and integration domain are changed to those of the reference unit cube by the trilinear transformation, $\vec{X} = \vec{r}(p, q, r)$, and the determinant of the Jacobian of the transformation, $\det \mathbf{J} \equiv \left| \frac{\partial(x,y,z)}{\partial(p,q,r)} \right|$. Thus, the volumetric integral, $\mathcal{I}$, in the physical space (x, y, z), is calculated as function of the coordinates in the canonical space (p, q, r) as:

$$\mathcal{I} = \int_0^1 \int_0^1 \int_0^1 g(\vec{r}(p, q, r)) \det \mathbf{J} \, \mathrm{d}p \, \mathrm{d}q \, \mathrm{d}r \tag{25}$$

where the Jacobian, $\det \mathbf{J}$, is clearly a function of the location (p, q, r).

The triple integral of Equation (25) is evaluated numerically by applying Gauss-Legendre quadrature integration rules for the specified level of accuracy. For a quadrature rule with N_v volumetric Gauss points, $\mathcal{I}$ in Equation (25) is approximated as

$$\mathcal{I} \simeq \sum_{m=1}^{N_v} g\left(\vec{r}(p, q, r)\right) (\det \mathbf{J})_m \, \omega_m = \sum_{m=1}^{N_v} g(\vec{X}_m) \tilde{\omega}_m \tag{26}$$

where $\vec{X}_m = \vec{r}(p_m, q_m, r_m)$ and $\tilde{\omega}_m = (\det \mathbf{J})_m \, \omega_m$ represent the Gauss-Legendre abscissa and weight in the physical space. Note that the abscissa $\vec{X}_m$ is the trilinear transformation image of the abscissa (p_m, q_m, r_m) in the reference unit cube and the weight $\tilde{\omega}_m$ is determined as the product between the local Jacobian and the corresponding Gaussian weight coefficient ω_m. The volumetric weights ω_m at a given point (p, q, r) in Cartesian coordinates are given by the tensor product of the one-dimensional Gauss-Legendre weights in each direction.

Note also that $\left(\vec{X}_m, \tilde{\omega}_m\right)$ depend only on the hexahedral cell geometry. In this work we opt to store and reuse them for volumetric integrations involving different $g(\vec{X})$ functions (e.g., calculation of volume, centroid, geometric moments etc.). An analogous approach is followed for the integration of variables over a hexahedron face.

American Institute of Aeronautics and Astronautics

E.   Flux Evaluation

1.   Inviscid Flux

Once the solution is reconstructed to the desired order of accuracy at the cell boundary, the inviscid flux calculation can be performed by the solution of a Riemann problem[42] between the states given by the reconstruction of the solution on each cell adjacent to the boundary. The accuracy of the integration method used to integrate the flux numerically should, therefore, not degrade the spatial accuracy given by the reconstruction method. In this work The AUSM+-up approximate Riemann solver of Liou[43] is used.

2.   Viscous Flux

The viscous fluxes depend on both the solution states and the solution gradients at the cell interfaces:

$$\vec{\mathcal{F}}^{\mathrm{V}} \cdot \overrightarrow{n} = \vec{\mathcal{F}}^{\mathrm{V}}(\, \mathbf{U}_{left}, \, \nabla \mathbf{U}_{left}, \, \mathbf{U}_{right}, \, \nabla \mathbf{U}_{right}, \, \overrightarrow{n}, \, \eta = 0 \,) \,. \tag{27}$$

The discretization procedure used in this work, follows directly from the work of Ivan and Groth in two dimensions.[44] The unlimited reconstructed solution state and gradients are calculated at the quadrature points at the boundary for both cells adjacent to the boundary. The cell boundary solution value and gradient are calculated as the arithmetic means of the left and right state and gradient values.[44] Gauss quadrature is performed following the rationale presented on section D to obtain the total flux for each face.

The reconstruction polynomial defined in Equation (22) can be directly differentiated in each direction, so that, for example, in the x-direction we arrive at the following expression for the gradient

$$\frac{\partial U_{ijk}^k(x,y,z)}{\partial x} = \sum_{\substack{p_1=0 \\ (p_1+p_2+p_3 \leq k)}}^{k} \sum_{p_2=0}^{k} \sum_{p_3=0}^{k} p_1 (x-x_i)^{p_1-1}(y-y_i)^{p_2}(z-z_i)^{p_3} D_{p_1 p_2 p_3} \,, \tag{28}$$

Analogous expressions are derived for $\frac{\partial U_{ijk}^k(x,y,z)}{\partial y}$ and $\frac{\partial U_{ijk}^k(x,y,z)}{\partial z}$. Considering again the cell interface in the x-direction the arithmetic means of both the solution and its gradients are obtained as follows:

$$U_{i+\frac{1}{2},j,k} = \frac{(U_{left} + U_{right})}{2} \,, \tag{29}$$

$$\nabla U_{i+\frac{1}{2},j,k} = \frac{(\nabla U_{left} + \nabla U_{right})}{2} \,. \tag{30}$$

Equation (28) for the solution gradient has a leading truncation error term which is one order less than the kth-order reconstruction polynomial, given by Equation (22). As such, in order to obtain a kth-order accurate spatial discretization (for elliptic operators and the Navier-Stokes equations), a kth-order reconstruction polynomial is used. To achieve a fourth-order scheme, piecewise quartic reconstruction, with $k = 4$, is therefore required.

VI.   Numerical Results

### A.   High-Order Reconstruction of Prescribed Functions

1.   Smooth Trigonometric Function

Prior to preceding with the LES reactive flow computations, verification of the high-order CENO solution reconstruction for three-dimensional Cartesian as well as general hexahedral meshes was first considered by studying the reconstruction of prescribed functions. Remembering that a hexahedral cell may in general have non-planar faces, the general hexahedral meshes were obtained here by randomly perturbing originally uniform Cartesian meshes. As a first case, reconstruction of a radial cosine function was examined on a solution domain of size $(20\,m \times 20\,m \times 20\,m)$. For this smooth and continuous function, the goal was to establish that the expected order of accuracy on hexahedral elements. Furthermore, as the reconstruction process relies on the evaluation of volumetric integrals for the cell volume itself and centroid locations, as well as to integrate the geometric moments required to construct the least-squares problem for the reconstruction,

American Institute of Aeronautics and Astronautics
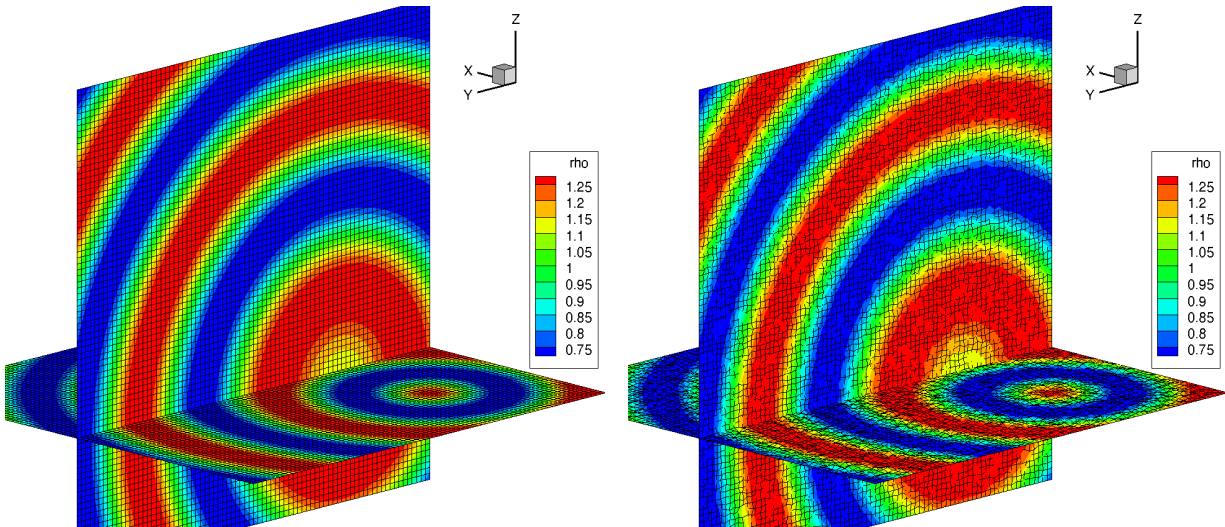
(a) Cut planes showing radial cosine function reconstructed on Cartesian mesh (CENO 5th) order

(b) Cut planes showing radial cosine function reconstructed on hexahedral mesh (CENO 5th) order

Figure 2. Cut planes comparing the 5th order reconstruction function working on hexahedral (disturbed) mesh as expected in comparison to the Cartesian mesh
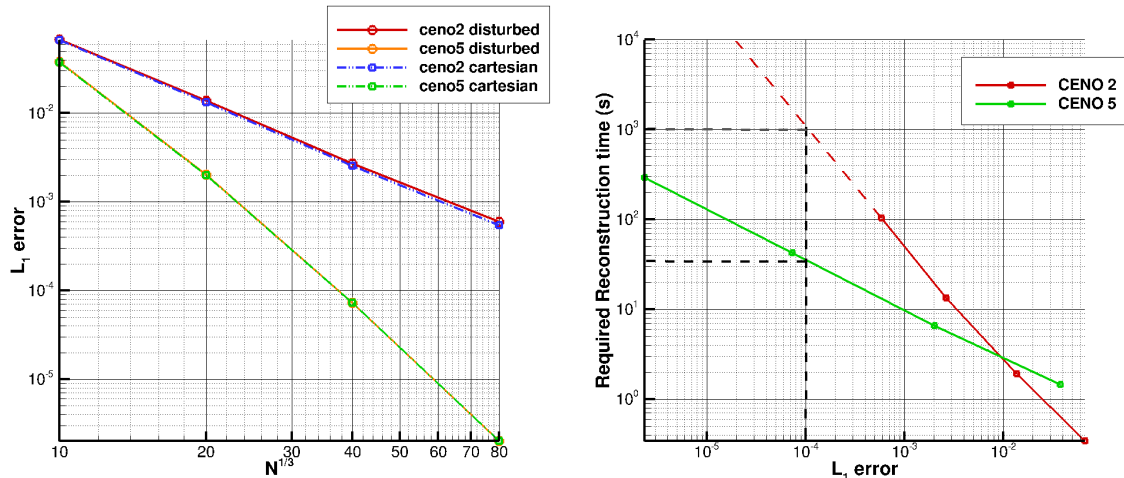

(a) Error Analysis for Radial Cosine function using 2nd and 5th order accuracy on Cartesian and hexahedral (disturbed) mesh

(b) Analysis of time required to achieve a desired error level with a given reconstruction. Comparison between 2nd and 5th order.

Figure 3. Error Analysis demonstrating proper order of accuracy for the CENO scheme in a disturbed mesh and time required for desired error level based on order of the reconstruction.

this test case also provided a confirmation of the effectiveness of the trilinear transformation and volumetric quadrature for the hexahedral elements.

The distributions of the reconstructed radial cosine function on both three-dimensional Cartesian and hexahedral meshes are illustrated in Figure 2. Furthermore, it is shown in Figure 3(a) that the expected order of accuracy of the $k = 2$ and $k = 4$ schemes is achieved on both regular and perturbed meshes. An interesting result is also found by comparing the time required to perform the solution reconstruction with different orders of accuracy for the meshes considered as depicted in Figure 3(b). One can see that for a given error the time required by the second-order scheme may be orders of magnitude higher than the time required by the fifth-order scheme.

American Institute of Aeronautics and Astronautics
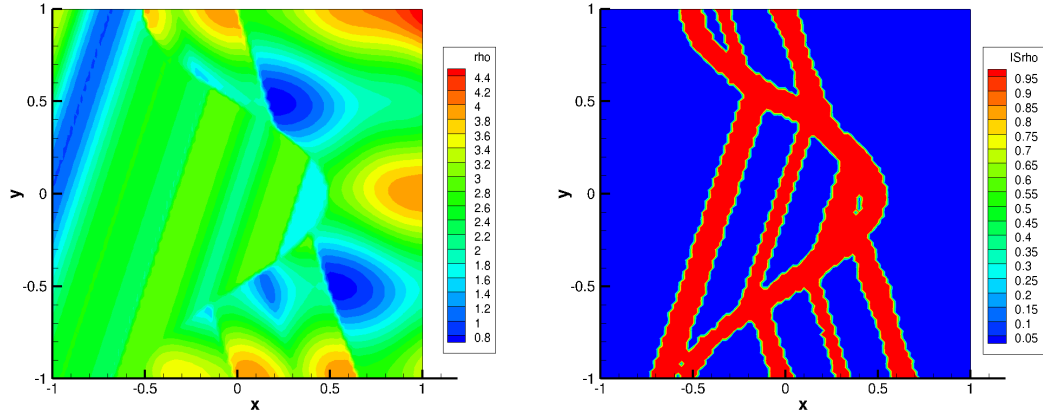
(a) Fifth-Order CENO reconstruction on a hexahedral (disturbed) mesh - contour of ρ for Abgrall function

(b) Fifth-Order CENO reconstruction on a hexahedral (disturbed) mesh - contour of the smoothness indicator for variable ρ for the Abgrall function

Figure 4. Demonstration of the smoothness indicator use with disturbed hexahedral cells flagging the discontinuos regions in the field of variable ρ for the Abgrall function.

2. Non-Smooth Abgrall Function

In order to investigate the CENO solution reconstruction procedure for non-smooth function, the Abgrall function[45] was considered. By construction, this function contains several solution discontinuities in order to present challenges to any reconstruction scheme hoping to enforce solution monotonicity. For this case, the functionality and reliability of the smoothness indicator used in the hybrid CENO reconstruction procedure is also demonstrated. While this ability has been extensively tested in other previous work, and the main goal here was to show that consistent results can also be obtained using general hexahedral elements.

Considering the number of discontinuous regions within the domain, as shown in Figure 4(b), it is expected that our high-order hybrid scheme switches to a low-order mode in a high number of cells bringing down the overall order of accuracy. Although that is true, one can see from Figure 5 that, while the high-order scheme exhibits a grid-convergence rate or order of accuracy (slope) that similar to the first-order scheme, it is also evident that the absolute value of the error for the high-order reconstructed solution is considerably smaller than that of the usual first-order scheme. For a the target solution error given in the figure, a much fewer number of cells ($100 \times 100 = 10,000$) is required by the high-order to scheme to achieve the same accuracy as the first-order scheme on a fine mesh ($180 \times 180 = 32,400$). Extrapolating this result to the three-dimensional case, the ratio $(180^3)/(100^3)$ indicates that about 5.8 times more cells would be required by the low-order scheme to return the same level of error as the high-order approach. ,

B. Non-Reactive Inviscid Flow — Wave Propagation

The implementation of the high-order inviscid flux function was also verified here by solving a simple wave propagation problem in a periodic domain. A periodic sinusoidal field was initialized for the density, ρ, and a uniform x-direction velocity of $u=100$ m/s was applied. The magnitude of the velocity components in the y and z directions was taken to be zero and a uniform pressure of $p=101,325$ Pa was assumed. The expected exact solution for density, ρ, after a full period (20ms) is the same initial wave convected without the lags in phase or amplitude decays associated with the numerical discretization scheme.

The numerical results presented in Figures 6(a) and 6(b) demonstrate that valid solutions were obtained for both Cartesian and hexahedral meshes. In both cases, the initial wave shape is recovered. Ivan et al[38] have also shown that the desired orders of accuracy (up to 4th) can be obtained for this case.
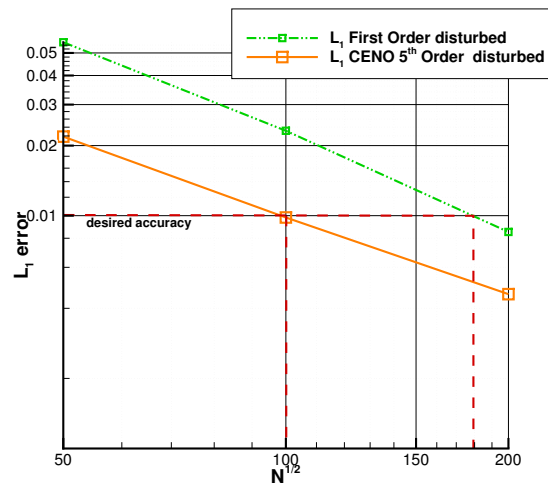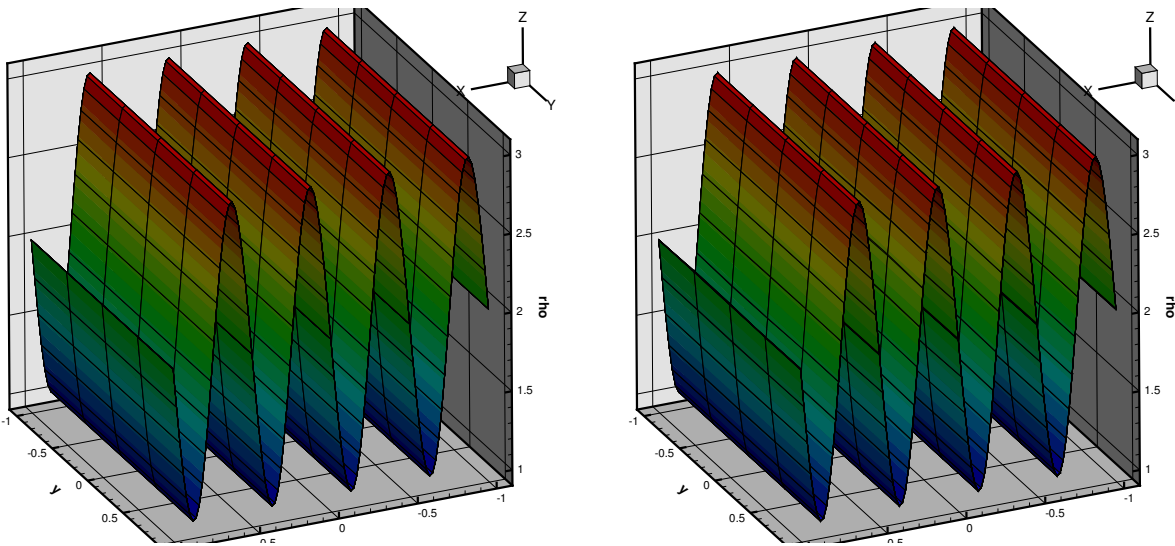
Figure 5. Comparison of L$_1$-error obtained with first and fifth-order reconstruction. Dashed lines exemplify the smaller number of cells required by high-order scheme for a given error, despite slopes being similar due to large number of cells flagged as discontinuous.

(a) Fifth-Order CENO on a Cartesian mesh - solution after one full cycle (20ms) - 100 elements in x-direction

(b) Fifth-Order CENO on a hexahedral (disturbed) mesh - solution after one full cycle (20ms) - 100 elements in x-direction

Figure 6. Contour plot of a sinusoidal density wave travelling in x-direction at constant speed $u = 100$ m/s. Comparative demonstration of solution using hexahedral and Cartesian cells.

C. Non-Reactive Inviscid Flow — Shock-Cube Problem

The high-order CENO scheme is further verified through application to an inviscid three-dimensional shock-box problem in which both both uniform Cartesian and distorted hexahedral computational mesh were considered. This problem is a generalization of the one-dimensional shock-tube problem for a 1 $m{\times}1\ m{\times}1\ m$ three-dimensional domain.

Figures 7(a) and 7(b) show the matching density variation on two cut planes of constant z coordinates for the Cartesian and hexahedral mesh. Figures 8(a) and 8(b) demonstrate the same regions are flagged (in red) by the smoothness indicator as regions of the solution having under-resolved or discontinuous features for both meshes.
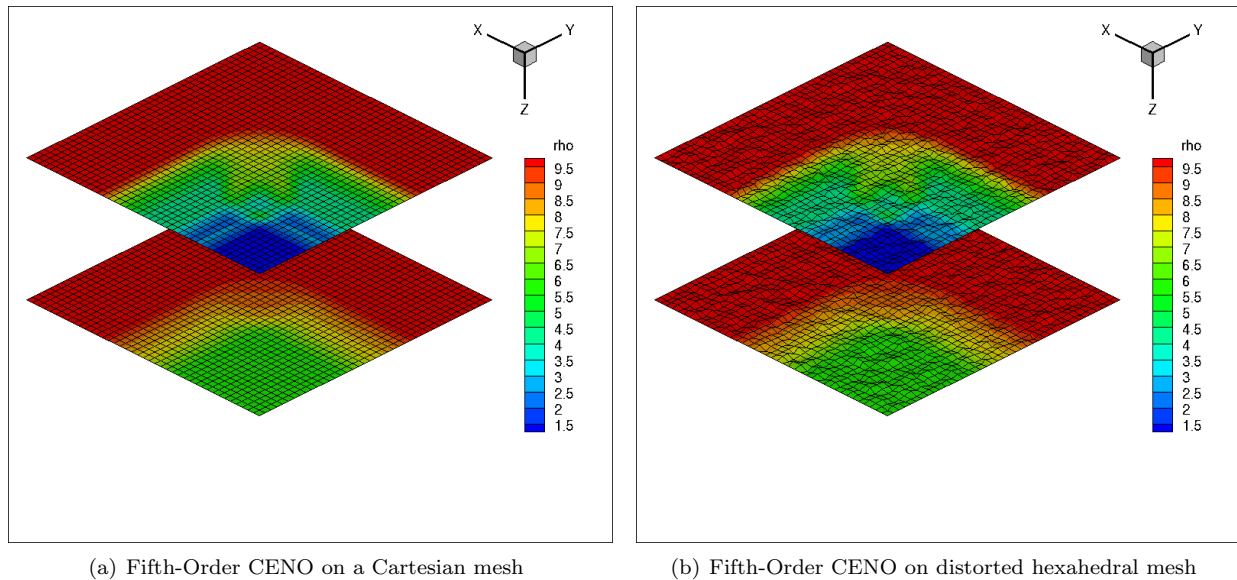
American Institute of Aeronautics and Astronautics

(a) Fifth-Order CENO on a Cartesian mesh   (b) Fifth-Order CENO on distorted hexahedral mesh

Figure 7. Density variation for the shock-box problem shown on selected cut planes in the domain: $t = 0.5\,ms$, $40^3\,grid$**.**

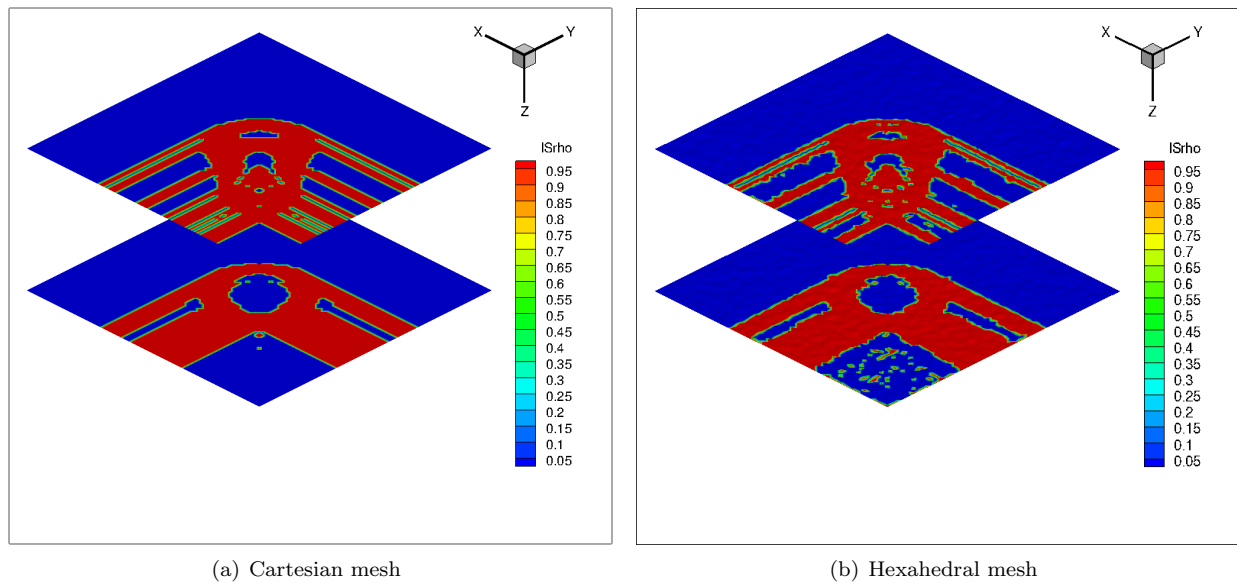(a) Cartesian mesh   (b) Hexahedral mesh

Figure 8. Contours of smoothness indicator for variable ρ flagging the discontinuities in the solution which shall be solved by the reduced order scheme to enforce monotonicity

D. Non-Reactive Viscous Flow — Decay of Isotropic Turbulence

Finally, to verify the high-order implementation of the viscous fluxes using LES before preceding to the reactive flow cases, the decay of a three-dimensional homogeneous isotropic turbulence field was considered. It should be noted that the rate of decay of the isotropic turbulence is expected to be proportional to $t^{-1.25}$, according to both experiments and DNS results.[46] A $(2\pi\,m \times 2\pi\,m \times 2\pi\,m)$ solution domain was considered and an isotropic turbulence field was introduced, following the methodology presented by Rogallo.[47] The boundaries of this solution domain are assumed to be periodic in all directions. Following other previous grid convergence studies,[48,49] the turbulence decay was evaluated using two grid sizes comprising of $(32 \times 32 \times 32)$ cells and $(64 \times 64 \times 64)$ cells. The Smagorinsky SFS model[12] was used as in all cases.
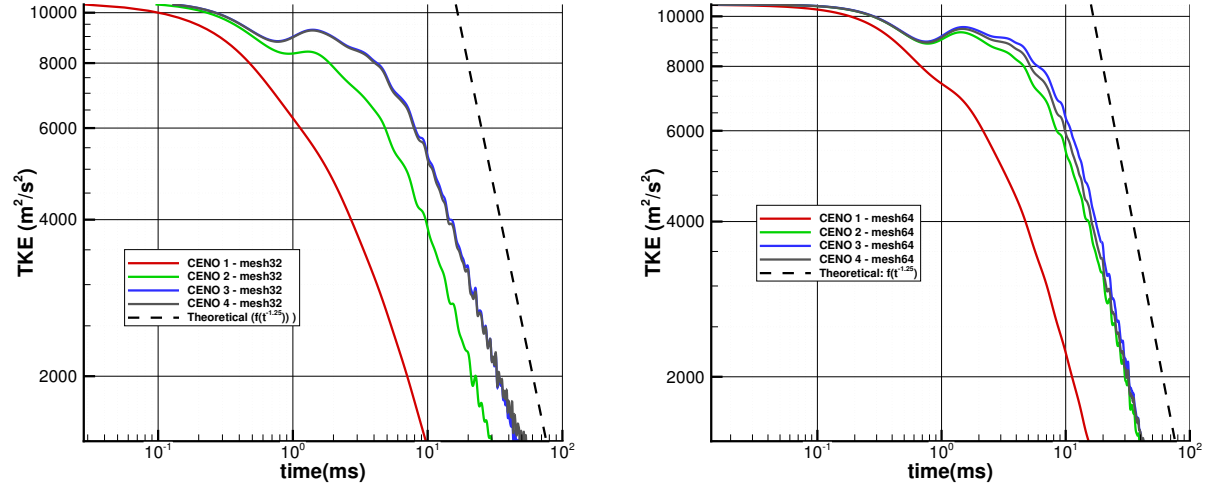
(a) Decay of Turbulent Kinetic Energy on $(32 \times 32 \times 32)$ mesh for several spatial discretization schemes

(b) Decay of Turbulent Kinetic Energy on $(64 \times 64 \times 64)$ mesh for several spatial discretization schemes

Figure 9. Comparison of the Decay of Isotropic Turbulence using the high-order implementation of the viscous fluxes

The simulation results presented in Figures 9(a) and 9(b) show the LES predictions of decay of the isotropic turbulent field within the domain as obtained by proposed the proposed finite-volume scheme on the two meshes. Results are presented for various orders, without monotonicity enforcement, so as to highlight the effect of the increasing accuracy order of the scheme on the preservation of turbulent content in the domain. As expected the results for the $(64 \times 64 \times 64)$ mesh are slightly improved and provide a better representation of the decay process than the $(32 \times 32 \times 32)$ mesh. Also, it can be seen that by refining the mesh, the different schemes (2nd, 3rd and 4th-orders) converge to a similar decay rate and absolute value of total turbulent kinetic energy profile.

E. Freely Propagating Premixed Methane-Air Flame in an Isotropic Turbulent Field

The first assessment of the high-order CENO scheme applied to LES with PCM-FPI implementation for reactive flows was made by studying the numerical solution of freely propagating methane-air flames in a cubic domain. The LES reactive flow simulations are performed by superimposing a decaying isotropic and homogeneous turbulent field to a planar laminar premixed flame inside a three dimensional box. The homogeneous isotropic turbulent flow field was initialized by again making use of Rogallo's turbulence initialization procedure[47] and the model spectrum proposed by Haworth and Poinsot.[50] LES results were obtained using both second-order spatial discretization scheme (CENO 2) and the fourth-order method (CENO 4). Additionally, results for two different meshes were obtained: a $(32 \times 32 \times 32)$ and $(64 \times 64 \times 64)$ mesh were both used. The computaional domain was a cube of size $(0.01m \times 0.01m \times 0.01m)$ and subsonic inflow and outflow boundary conditions were applied on the constant x faces and periodic boundary conditions were enforced on the other four faces. The particular conditions for the premixed flame of interest are summarized in Table 1. The turbulence intensity was such that the flame lies in the thin reaction zone regime of turbulent premixed combustion diagram,[51] just above the flamelet regime limit.

Figure 10 provides the predicted evolution of the turbulent burning rate, S_T, non-dimensionalized by the

ϕ	Λ	λ	η	u'	s_{L}	δ_{L}	u'/s_{L}	$\Lambda/\delta_{\mathrm{L}}$
	mm	mm	mm	m/s	m/s	mm		
0.7	1.790	0.460	0.02935	2.92	0.201	0.11	14.38	16.64

Table 1. Summary of turbulence scales and flow conditions for case N

American Institute of Aeronautics and Astronautics
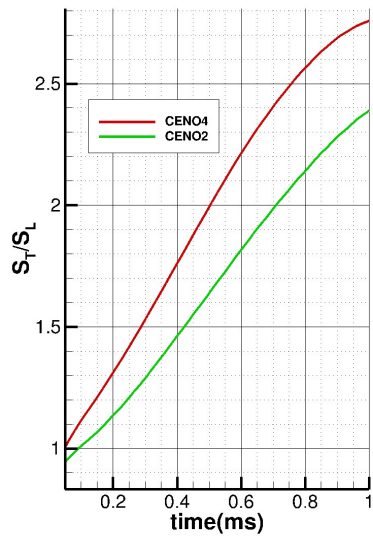
(a) Burning rate adimensionalized by laminar speed for the $(32 \times 32 \times 32)$ mesh
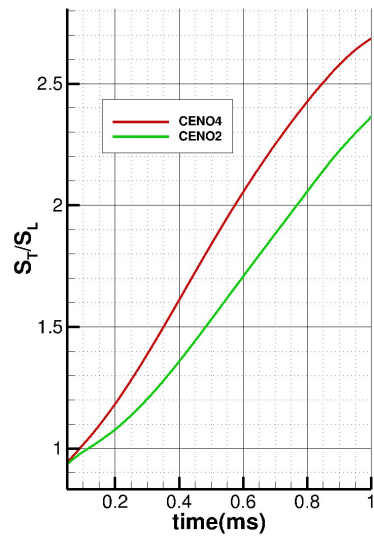
(b) Burning rate adimensionalized by laminar speed for the $(64 \times 64 \times 64)$ mesh

Figure 10. Comparison of 4th and 2nd order results for the burning rate evolution in time, showing the higher levels achieved with the high-order scheme on both meshes
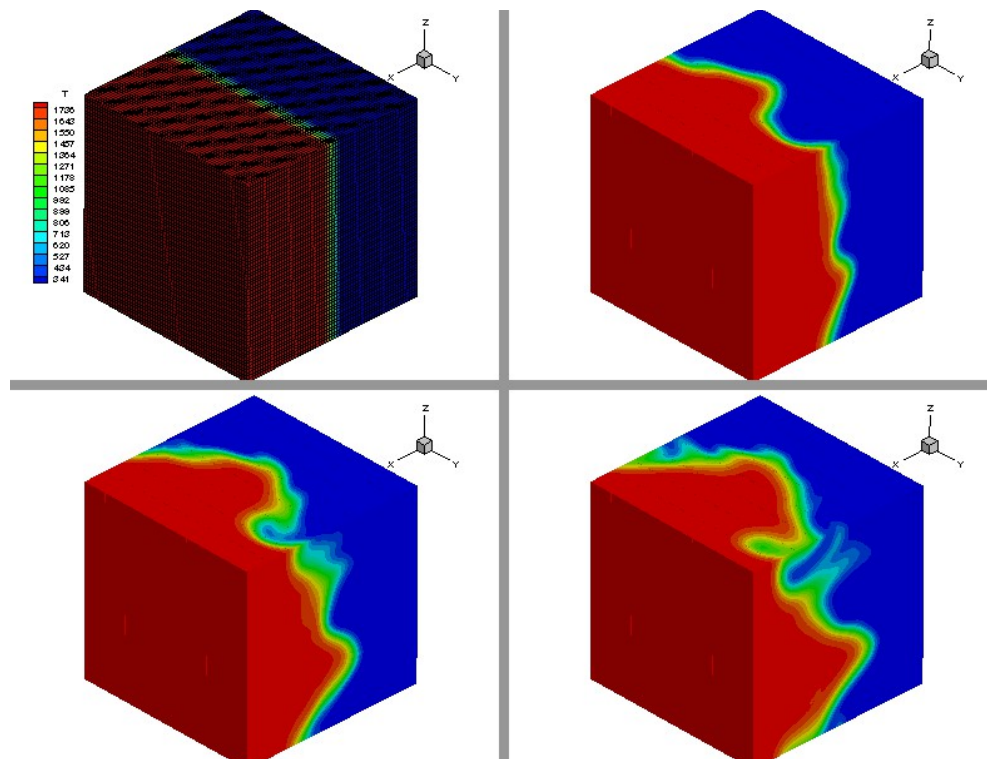

Figure 11. Time evolution of temperature contours for CENO4 (mesh 64, t=0ms, 0.25ms, 1ms and 4ms)

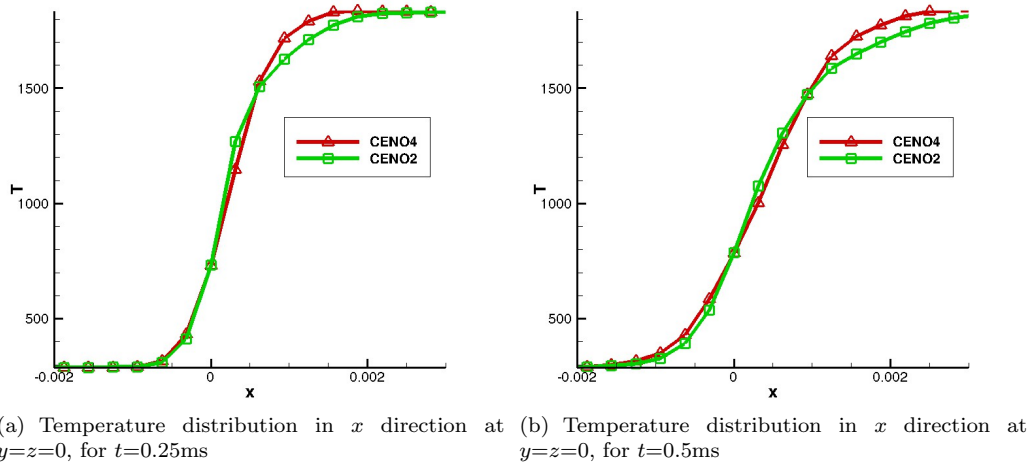American Institute of Aeronautics and Astronautics

(a) Temperature distribution in x direction at $y=z=0$, for $t=0.25$ms

(b) Temperature distribution in x direction at $y=z=0$, for $t=0.5$ms

Figure 12. Comparison of 4th and 2nd order temperature distribution

laminar flame speed, S_L, obtained in the LES simulations as a function of time. Results for the second- and fourth-order spatial schemes are compared. In both cases, an explicit, fourth-order, Runge-Kutta, time-marching scheme was used. It can be seen that the high-order spatial scheme predicts a higher turbulent burning rate when compared to the second-order scheme for both meshes.

Figure 11 shows the evolution of predicted temperature contours in time, demonstrating the flame wrinkling increasing as the reaction progress. Contours are shown for $t=0$ms (top left), $t=0.25$ms (top right), $t=0.5$ms (bottom left) and $t=0.75$ms (bottom right). A closer look at the temperature distribution for the
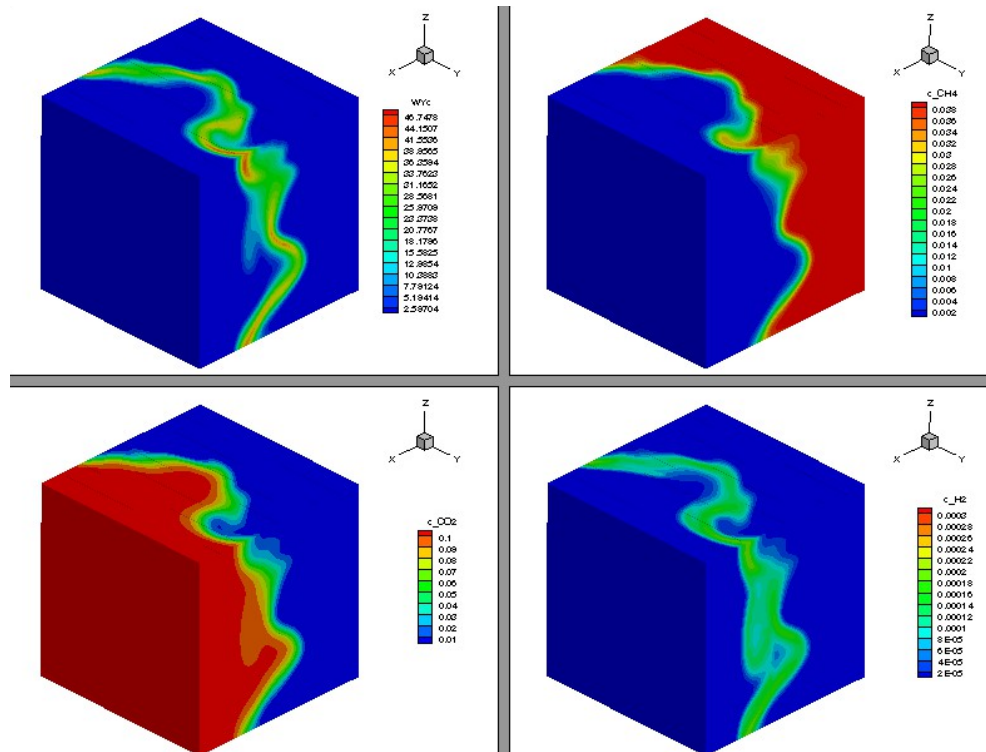

Figure 13. Contours of progress variable production and mass fractions of CH_4, CO_2 and H_2, @ $t=0.5$ms (CENO4, mesh 64)

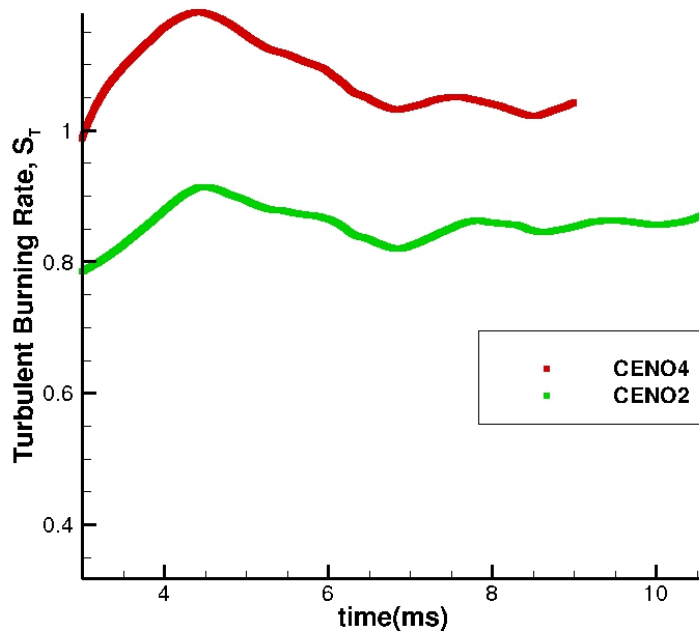American Institute of Aeronautics and Astronautics

Figure 14. Burning rate comparison for the second-order and fourth-order schemes

$(32 \times 32 \times 32)$ mesh along x direction at constants $y=z=0$ is shown in Figures 12(a) and 12(b), for times $t=0.25$ms and $t=0.50$ms respectively. In these plots a detail of the sharper gradient representation provided by the high-order reconstruction is given.

Figure 13 shows the contours of the production of the progress variable (top left) and the contours of species mass fractions for CH_4, CO_2 and H_2, at $t=0.5$ms for the $(64 \times 64 \times 64)$ mesh. The production of progress variable contours allowd one to identify the reaction front, or the region where CO and CO_2 are being produced. The presence of CH_4 predominantly in the reactants and CO_2 predominantly in the products region is also observed. Moreover it is possible to detect the concentration of H_2 mostly confined to the reacting front and decaying to zero as one moves toward either the reactants or products.

F.   Laboratory-Scale Premixed Methane-Air Bunsen Flame

The axisymmetric Bunsen flame and burner geometry studied previously by Shahbazian *et al*[16] was also studied here. In the previous work, different subfilter scale models for turbulence-chemistry interaction were compared to the available experimental data of Yuen and Gülder.[52] The same turbulent flow conditions described in Table 1 were used in one of the Bunsen flame cases of this previous work. It is this case that is also consdered here.

Figure 14 depicts the predictions of the global burning rate for the lean premixed flame obtained using LES with both the second- and fourth-order finite-volume schemes. It is possible to notice that the high-order scheme applied to the lean premixed Bunsen flame yields a higher burning rate than the second-order scheme. This result is consistent with what was seen for the freely propagating flame in the previous examples. The progress variable contours obtained from time averaging of the LES solution once the burning rate achieves a quasi-steady value are shown in Figure 15. The fine mesh (about 1.7 million elements) and second-order results are reproduced here from the study of Shahbazian *et al*[16] and are shown in Figure 15(a). In order to make a first assessment of the performance of the fourth-order scheme, a coarse mesh (about 170,000 elements) was also used and LES results were obtained using both the second- and fourth-order CENO schemes. In Figure 15(b), the results obtained for the coarse mesh using the second-order scheme are shown, which are clearly over-predicting the flame height when compared to the fine mesh second-order result. The results for the high-order scheme with this same coarse mesh are depicted in Figure 15(c). It can be seen
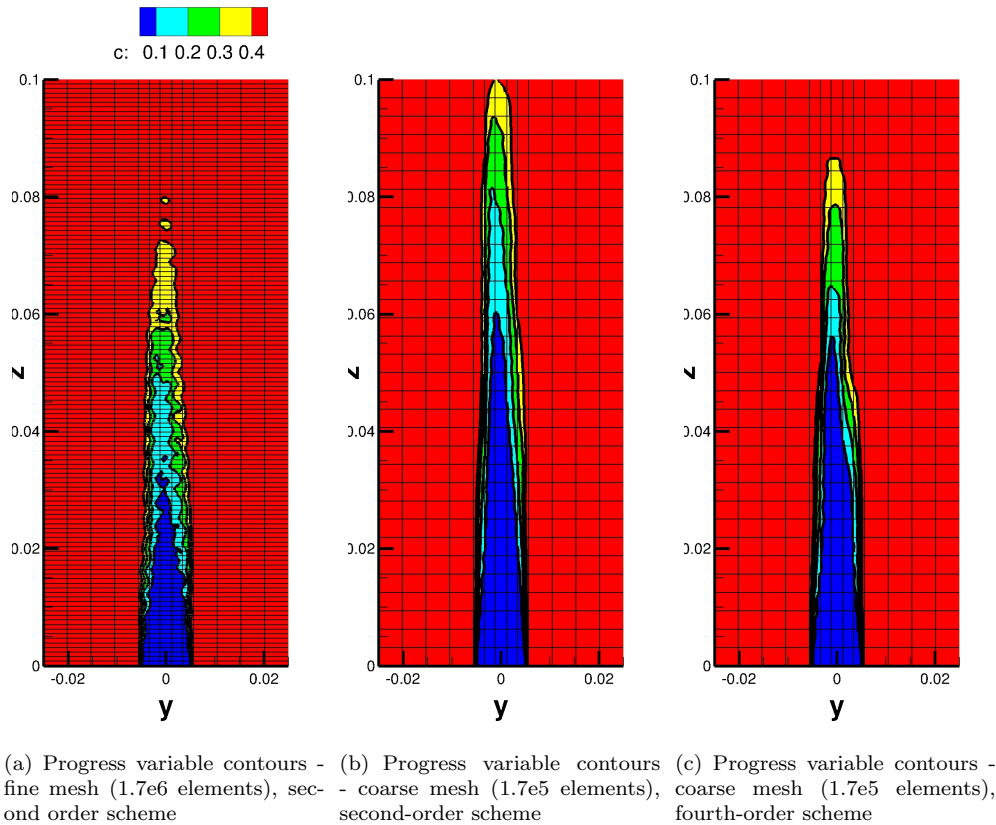
American Institute of Aeronautics and Astronautics

(a) Progress variable contours - fine mesh (1.7e6 elements), second order scheme

(b) Progress variable contours - coarse mesh (1.7e5 elements), second-order scheme

(c) Progress variable contours - coarse mesh (1.7e5 elements), fourth-order scheme

Figure 15. Contours of normalized progress variable c for different meshes and spatial schemes

that the flame obtained with the high-order scheme is lower than that obtained for the second-order scheme on the coarser mesh and in better agreement with the fine-mesh second-order results.

The predicted average flame heights for the three numerical results described above are compared to the estimated experimental flame height obtained by Yuen and Gülder[52] in Figure 15. Contours for the normalized progress variable at $c = 0.4$ are shown. Again, it can be seen that the finer spatial scheme performs better than the second-order for the same coarse mesh, moving the solution closer to the experiments and to that obtained with the second-order scheme with a mesh about 10 times finer.

VII.   Concluding Remarks

A high-order CENO finite-volume scheme, based on the previous work of Ivan and Groth[9,10] for non-reactive flows in two space dimensions, has been developed and applied to LES of turbulent premixed flames. Details of the proposed high-order CENO scheme applied to the Favre-filtered form of the Navier-Stokes equations for a compressible gaseous reactive mixture with a PCM-FPI turbulence-chemistry interaction combustion model were discussed and described. Numerical results that examine the underlying features of the proposed high-order scheme were presented and some preliminary results for LES of turbulent premixed flames were assessed. In general, the proposed high-order CENO finite-volume scheme proved promising for LES of reactive flows, outperforming the standard second-order scheme in several respects. Nevertheless, further study of the high-order approach for a broader range of reactive flows is certainly warranted and will be the subject of future follow-on research.
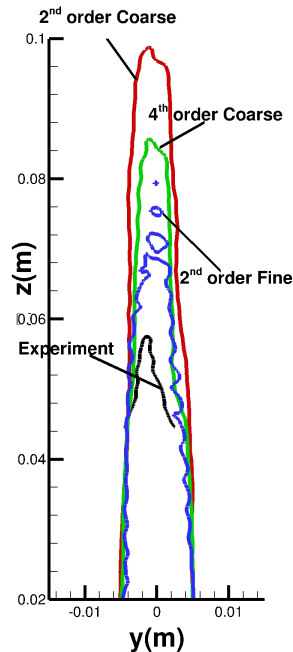
American Institute of Aeronautics and Astronautics

Figure 16. Flame height comparison for lean Bunsen burner case with different schemes (contours of progress variable $c=0.4$)

Acknowledgments

The first author would like to thank Embraer S.A. and CNPq-Brazil (Science Without Borders program - project number 201917/2012-2) for the financial support. Financial support for the research described herein was provided by the MITACS (Mathematics of Information Technology and Complex Systems) Network, part of the Networks of Centres of Excellence (NCE) program funded by the Canadian government. All fundings are gratefully acknowledged with many thanks. The computational resources for performing all of the calculations reported herein were provided by the SciNet High Performance Computing Consortium at the University of Toronto and Compute/Calcul Canada through funding from the Canada Foundation for Innovation (CFI) and the Province of Ontario, Canada.

References

[1]Bilger, R., "The Role of Combustion Technology in the 21st Century," *Turbulent Combustion Modeling Advances, New Trends and Perspectives*, edited by T. Echekki and E. Mastorakos, Fluid Mechanics and its Applications, Springer, 2011, pp. 3–18.

[2]van der Hoeven, S., Boersma, B., Jonker, H. J., and Roekaerts, D. J. E. M., "Development of a Large Eddy Simulation code for turbulent non-premixed jet flames," *2nd ECCOMAS Thematic Conference on Computational Combustion*, TU Delft, 2007.

[3]Albouze, G., Poinsot, T., and Gicquel, L. Y. M., "Chemical kinetics modelisation and LES combustion model effects on a perfectly premixed burner," *Compte Rendus de Mecanique*, Vol. 337, 6-7, 2009, pp. 318–328.

[4]Poinsot, T., "Using LES to study reacting flows and instabilities in annular combustion chambers," *8th International ERCOFTAC Symposium on Engineering Turbulence Modelling and Measurements (ETMM)*, 2010.

[5]Yaldizli, M., Mehravaran, K., and Jaberi, F., "Large-eddy simulations of turbulent methane jet flames with filtered mass density function," *Int. J. Heat Mass Trans.*, Vol. 53, No. 1112, 2010, pp. 2551 – 2562.

[6]Franzelli, B., Riber, E., Gicquel, L., and Poinsot, T., "Large Eddy Simulation modelling of combustion instabilities in a lean partially premixed swirled flame," *Combustion and Flame*, Vol. 159, 2012, pp. 621–637.

[7]Wang, C., Shu, C., Han, W., and Ning, J., "High resolution WENO simulation of 3D detonation waves," *Combustion and Flame*, Vol. 2, 2012, pp. 447–462.

[8]Fureby, C., "Large Eddy Simulation modelling of combustion for propulsion applications," *Phil. Trans. Royal Soc. London A*, Vol. 367, 2009, pp. 2957–2969.

[9]Ivan, L. and Groth, C. P. T., "High-Order Central ENO Finite-Volume Scheme with Adaptive Mesh Refinement," Paper 2007-4323, AIAA, June 2007.

American Institute of Aeronautics and Astronautics

[10]Ivan, L. and Groth, C. P. T., "High-Order Solution-Adaptive Central Essentially Non-Oscillatory (CENO) Method for Viscous Flows," Paper 2011-0367, AIAA, January 2011.

[11]Charest, M., Groth, C., and Gauthier, P., "High-Order CENO Finite-Volume Scheme for Low-Speed Viscous Flows on Three-Dimensional Unstructured Mesh," *Seventh International Conference on Computational Fluid Dynamics (ICCFD7)*, July 2012, p. 1.

[12]Smagorinski, J., "General Circulation Experiments with the Primitive Equations. I: The Basic Experiment," *Monthly Weather Review*, Vol. 91, No. 3, 1963, pp. 99–164.

[13]Schumann, U., "Subgrid scale model for finite difference simulations of turbulent flows in plane channels and annuli," *Journal of Computational Physics*, Vol. 18, No. 4, 1975, pp. 376 – 404.

[14]Yoshizawa, A., "Statistical theory for compressible turbulent shear flows, with the application to subgrid modeling," *Phys. Fluids A*, Vol. 29, 1986, pp. 2152–2164.

[15]Hernàndez-Pérez, F., Yuen, F., Groth, C., and Ö.L.Gulder, "LES of a laboratory-scale turbulent premixed Bunsen flame using FSD, PCM-FPI and thickened flame models," accepted in the Proceedings of the Combustion Institute, 2010.

[16]Shahbazian, N., Groth, C. P. T., and Gülder, O. L., "Assessment of Presumed PDF Models for Large Eddy Simulation of Turbulent Premixed Flames," Paper 2011-781, AIAA, January 2011.

[17]Gicquel, O., Darabiha, N., and Thévenin, D., "Laminar premixed hyrogen/air counterflow flame simulations using flame prolongation of ILDM with differential diffusion," *Proceedings of the Combustion Institute*, Vol. 28, 2000, pp. 1901–1908.

[18]Maas, U. and Pope, S., "Simplifying chemical kinetics: Intrinsic low-dimensional manifolds in composition space," *Combustion and Flame*, Vol. 88, No. 3-4, 1992, pp. 239 – 264.

[19]Goodwin, D. and Moffat, H. K., "Cantera," http://code.google.com/p/cantera/.

[20]Smith, G. P., Golden, D. M., Frenklach, M., Moriarty, N. W., Eiteneer, B., Goldenberg, M., Bowman, C. T., Hanson, R. K., Song, S., Gardiner, W. C., Lissianski, V. V., and Qin, Z., "GRI-Mech 3.0," http://www.me.berkeley.edu/gri_mech/.

[21]Cant, S., "RANS and LES Modelling of Premixed Turbulent Combustion," *Turbulent Combustion Modeling Advances, New Trends and Perspectives*, edited by T. Echekki and E. Mastorakos, Fluid Mechanics and its Applications, Springer, 2011, pp. 63–90.

[22]Galpin, J., Naudin, A., Vervich, L., Christian Angelberger, O. C., and Domingo, P., "Large-eddy simulation of a fuel-lean premixed turbulent swirl-burner," *Combustion and Flame*, Vol. 155, 2008, pp. 247–266.

[23]Fiorina, B., Baron, R., Gicquel, O., Vervisch, L., Carpentier, S., and Darabiha, N., "Modelling non-adiabatic partially premixed flames using flame-prolongation of ILDM," *Combustion Theory and Modelling*, Vol. 7, 2003, pp. 449–470.

[24]Jha, P. K. and Groth, C. P. T., "Evaluation of Flame-Prolongation of ILDM and Flamelet Tabulated Chemistry Approaches for Laminar Flames," *49th AIAA Aerospace Sciences Meeting including the New Horizons Forum and Aerospace Exposition*, Orlando, Florida, January 2011.

[25]Fiorina, B., Gicquel, O., Vervisch, L., Carpentier, S., and Darabiha, N., "Premixed turbulent combustion modeling using tabulated detailed chemistry and PDF," *Proceedings of the Combustion Institute*, Vol. 30, 2005, pp. 867–874.

[26]Haworth, D. and Pope, S., "Transported Probability Density Function Methods for Reynolds-Averaged and Large-Eddy Simulations," *Turbulent Combustion Modeling Advances, New Trends and Perspectives*, edited by T. Echekki and E. Mastorakos, Fluid Mechanics and its Applications, Springer, 2011, pp. 119–142.

[27]Vervisch, L., Hauguel, R., Domingo, P., and Rullaud, M., "Three facets of turbulent combustion modelling: DNS of premixed V-flame, LES of lifted nonpremixed flame and RANS of jet-flame," *Journal of Turbulence*, Vol. 4, 2004, pp. 1–36.

[28]Domingo, P., Vervisch, L., Payet, S., and Hauguel, R., "DNS of a premixed turbulent V flame and LES of a ducted flame using a FSD-PDF subgrid scale closure with FPI-tabulated chemistry," *Combustion and Flame*, 2005, pp. 566–586.

[29]Vervisch, L., "Study and modeling of finite rate chemistry effects in turbulent non-premixed flames," *Annual Research Briefs*, Center for Turbulence Research, 1992, pp. 411–429.

[30]Domingo, P., Vervisch, L., and Veynante, D., "Large-Eddy simulation of a lifted methane jet flame in a vitiated coflow," *Combustion and Flame*, Vol. 152, 2008, pp. 415–432.

[31]Fiorina, B., Gicquel, O., Vervisch, L., Carpentier, S., and Darabiha, N., "Premixed turbulent combustion modeling using tabulated detailed chemistry and PDF," *Proceedings of the Combustion Institute*, Vol. 30, 2005, pp. 867–874.

[32]Subramanian, V., Domingo, P., and Vervisch, L., "Large eddy simulation of forced ignition of an annular bluff-body burner," *Combustion and Flame*, Vol. 157, 2010, pp. 579–601.

[33]Bray, K. N. C., Champion, M., Libby, P. A., and Swaminathan, N., "Finite rate chemistry and presumed PDF models for premixed turbulent combustion," *Combust. Flame*, Vol. 146, 2006, pp. 665–673.

[34]Jin, B., Grout, R., and Bushe, W. K., "Conditional Source-Term Estimation as a Method for Chemical Closure in Premixed Turbulent Reacting Flow," *Flow Turbulence Combust.*, Vol. 81, 2008, pp. 563–582.

[35]Barth, T. J. and Fredrickson, P. O., "Higher Order Solution of the Euler Equations on Unstructured Grids Using Quadratic Reconstruction," Paper 90-0013, AIAA, January 1990.

[36]Barth, T. J., "Recent Developments in High Order K-Exact Reconstruction on Unstructured Meshes," Paper 93-0668, AIAA, January 1993.

[37]Ivan, L. and Groth, C. P. T., "High-Order Central ENO Finite-Volume Scheme with Adaptive Mesh Refinement," Paper 2007-4323, AIAA, June 2007.

[38]Ivan, L., Susanto, A., Sterck, H. D., and Groth, C., "High-Order Central ENO Finite-Volume Scheme for MHD on Three-Dimensional Cubed-Sphere Grids," *Seventh International Conference on Computational Fluid Dynamics (ICCFD7)*, July 2012, p. 1.

[39]Zienkiewicz, O. and Taylor, R., *The Finite Element Method*, Vol. 1, Butterworth-Heinemann, 5th ed., 2000.

[40]Naff, R., Russell, T., and Wilson, J., "Shape functions for velocity interpolation in general hexahedral cells," *Computational Geosciences*, Vol. 6, 2002, pp. 285–314.

[41]Felippa, C. A., "A compendium of FEM integration formulas for symbolic work," *Eng. Comput.*, Vol. 21, No. 8, 2004, pp. 867–890.

[42]Toro, E. F., *Riemann Solvers and Numerical Methods for Fluid Dynamics: A Practical Introduction*, Springer, University of London, London, 2009.

[43]Liou, M.-S., "A Sequel to AUSM, Part II: AUSM$^+$-up for all speeds," *J. Comput. Phys.*, Vol. 214, 2006, pp. 137–170.

[44]Ivan, L. and Groth, C. P. T., "High-Order Central ENO Finite-Volume Scheme for the Advection-Diffusion Equation," *Proceedings of the 16th Annual Conference of the CFD Society of Canada, Saskatoon, Canada, June 9–11, 2008*, CFD Society of Canada, 2008.

[45]Abgrall, R., "On Essentially Non-Oscillatory Schemes on Unstructured Meshes: Analysis and Implementation," *J. Comput. Phys.*, Vol. 114, 1994, pp. 45–58.

[46]Deconinck, W., *Design and Application of Discrete Explicit Filters for Large Eddy Simulation of Compressible Turbulent Flows*, Master's thesis, University of Toronto, 2012.

[47]Rogallo, R. S., "Numerical Experiments in Homogeneous Turbulence," NASA Technical Memorandum 81315, 1981.

[48]Rashad, R., *Development of a High-Order Finite-Volume Method for the Navier-Stokes Equations in Three Dimensions*, Master's thesis, University of Toronto, 2009.

[49]Regmi, P., *A High-Order Finite-Volume Scheme for Large-Eddy Simulation of Premixed Flames on Multi-Block Cartesian Mesh*, Master's thesis, University of Toronto, 2012.

[50]Haworth, D. C. and Poinsot, T. J., "Numerical simulations of Lewis number effects in turbulent premixed flames," *J. Fluid Mech.*, Vol. 244, 1992, pp. 405–436.

[51]Peters, N., "The turbulent burning velocity for large-scale and small-scale turbulence," *J. Fluid Mech.*, Vol. 384, 1999, pp. 107–132.

[52]Yuen, T. and Gülder, O., "Premixed turbulent flame front structure investigation by Rayleigh scattering in the thin reaction zone regime," *Proceedings of the Combustion Institute*, Vol. 32, 2009, pp. 1747–1754.

American Institute of Aeronautics and Astronautics